ACS NANO

www.acsnano.org

ARTICLE

Optical Properties of Few-Layer Ti_3CN MXene: From Experimental Observations to Theoretical Calculations

Lingfeng Gao,*,▽ Hualong Chen,▽ Artem V. Kuklin,▽ Swelm Wageh, Ahmed A. Al-Ghamdi, Hans Ågren,* and Han Zhang*

Cite This: *ACS Nano* 2022, 16, 3059−3069

Read Online

ACCESS | Metrics & More | Article Recommendations | Supporting Information

ABSTRACT: **Despite the emerging interest in research and development of Ti_3CN MXene nanosheet (NS)-based optoelectronic devices, there is still a lack of in-depth studies of the underlying photophysical processes, like carrier relaxation dynamics and nonlinear photon absorption, operating in such devices, hindering their further and precise design. In this paper, we attempt to remedy the situation by fabricating few-layer Ti_3CN NSs *via* combining selective etching and molecular intercalation and by investigating the carrier relaxation possesses and broadband nonlinear optical responses *via* transient absorption and Z-scan techniques. These results are complemented by first-principle theoretical analyses of the optical properties. Both saturable absorption and reverse saturable absorption phenomena are observed due to multiphoton absorption effects. The analysis of these results adds to the understanding of the basic photophysical processes, which is anticipated to be beneficial for the further design of MXene-based devices.**

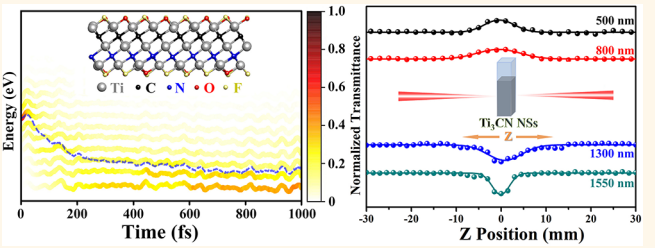

KEYWORDS: *Ti_3CN, MXene, transient absorption, Z-scan, density functional theory calculations*

Ever since the exfoliation of atomically thin graphene, two-dimensional (2D) materials have subverted multitudinous fields due to their extraordinary properties.[1] In the past decade, more than 20 different kinds of 2D materials have been reported, ranging from single elements to chemical compounds. Compared with the single-element 2D materials, compounds composed with multi-elements are generally more attractive, as the synergism and combination of various elements endow structural flexibility as well as intriguing properties.[2−6] For instance, owing to their superior electron mobility, transition-metal dichalcogenides (TMDs) have been successfully applied in broadband photodetectors with wavelengths ranging from ultraviolet to mid-infrared. These materials have been widely applied also in various other fields such as energy conversion, biomedicine, and catalysis.[7−11]

Among the family of 2D compounds, transition-metal carbides and nitrides hold a special place. They are commonly named as MXenes owing to the graphene-like structure and intimate relation to their MAX precursors[12−14] and are expressed with the universal formula of $M_{n+1}X_nT_x$ (n = 1−4), where M is an early transition metal, X refers to C/N, and T represents the surface terminations. The investigation of MXenes can be traced back to 2011 when Naguib *et al.* reported the Ti_3C_2 MXene.[15] Due to a large number of early transition metals, more than 40 MXenes have been experimentally developed, while hundreds of possibilities have been theoretically calculated.[16−19] However, more than 70% of the research has been focused on $Ti_3C_2T_x$ overshadowing the attention paid to other kinds of MXenes.[12]

Ti_3CN is a typical kind of hetero-MXene where half of the carbon content is substituted by nitrogen. The electronegative nitrogen gives stronger Ti−N bonding than Ti−C, resulting in enhanced physical and electronic properties. As revealed, the electronic conductivity and catalytic activity of N-containing MXenes are superior to those of the carbide ones due to the higher density of states at the Fermi level.[20] Ti_3CN was developed in 2012 and has been widely applied in rechargeable batteries, supercapacitors, and saturable absorbers.[21−23] However, there have only been a few works focusing on the detailed optical properties of Ti_3CN MXene, something that

Received: November 29, 2021
Accepted: January 14, 2022
Published: January 20, 2022

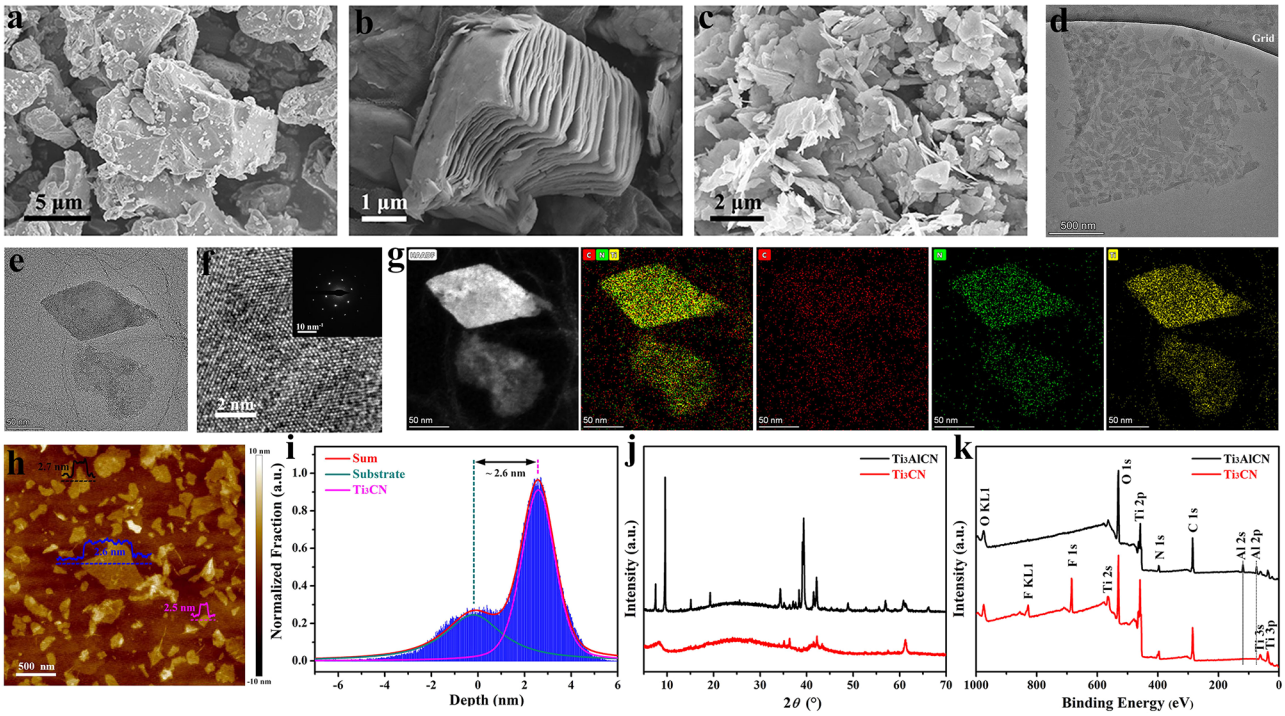

Figure 1. (a) SEM image of Ti_3AlCN MAX phase. (b) SEM image of HF-etched Ti_3CN MXene with multilayer structure. (c) SEM image of exfoliated Ti_3CN MXene with few-layer structure. (d) TEM image of aggregated few-layer Ti_3CN MXenes. (e) TEM image of individual few-layer Ti_3CN MXene. (f) HR-TEM of few-layer Ti_3CN MXene and insert is the SAED pattern. (g) Elemental mapping of few-layer Ti_3CN MXene. (h) AFM image of few-layer Ti_3CN MXene. (i) Summarized depth of few-layer Ti_3CN MXene based on the AFM image. (j) XRD patterns of Ti_3AlCN and Ti_3CN. (k) XPS spectra of Ti_3AlCN and Ti_3CN.

probably has slowed down its further development.[24] For instance, there is still a chasm between practical applications and fundamental understanding about carrier relaxation dynamics and nonlinear optical (NLO) response for Ti_3CN. Understanding the ultrafast relaxation dynamic is vital for investigating pulsed light−matter coupling phenomena.[25,26] For the NLO response, there are significant applications using the sizable third nonlinear susceptibility for ultrafast pulse generation in optoelectronic and photonic devices.[21,27,28]

To this concern, few-layer Ti_3CN nanosheets (NSs) with high quality have successfully been synthesized in this work *via* selective etching and molecular intercalation and structurally characterized by TEM, SEM, and AFM, while the composition has been confirmed by XRD, XPS, and EDS. The broadband ultrafast carrier relaxation processes of Ti_3CN were systemically investigated from visible (490−770 nm) to near-infrared (840−1240 nm) waveband regions with a time-resolved transient absorption (TA) instrument. A broadband ground-state bleaching signal ($\Delta A < 0$) was observed, and two different relaxation time components could be fitted. The broadband NLO response of Ti_3CN was studied with the well-known Z-scan technique by adjusting the laser intensity and wavelength. Both saturable absorption (SA) and reverse saturable absorption (RSA) phenomena could be observed. According to the intriguing results obtained, we envisage that 2D Ti_3CN NSs have promising potential for optoelectronic devices and with breakthrough capacity in this field.

RESULTS AND DISCUSSION

Synthesis of Few-Layer Ti_3CN MXenes. Taking the advantage of the high reactivity of Al−C bonds, large-scale MXenes can be fabricated by removing the Al layer from their MAX phases *via* an acid-etching approach. As can be seen in Figure 1a, the bulk Ti_3AlCN MAX phase shows a nonlayered feature, which hardly can be exfoliated by the traditional liquid-phase exfoliation method. After etching by hydrogen fluoride (HF) acid, the Al layer can be removed, and multilayer Ti_3CN with a slack accordion-like structure can be obtained (Figure 1b). In order to obtain few-layer Ti_3CN, the multilayer Ti_3CN was intercalated by tetramethylammonium hydroxide (TMAOH) molecules according to previous works.[29] Figure 1c demonstrates the SEM image of exfoliated Ti_3CN NSs which shows a few-layer feature. Due to the vigorous stirring process, the lateral dimension of the few-layer Ti_3CN NSs is significantly lower than that of multilayer Ti_3CN. A detailed elemental mapping analysis also confirmed the successful removal of the Al layer, where the elements of Ti, Al, C, and N can be observed in Ti_3AlCN, while only Ti, C, and N elements can be detected in multilayer Ti_3CN MXene (Figure S1). Figure 1d shows the TEM image of aggregated few-layer Ti_3CN NSs, and the electron-transparent flakes indicate an ultrathin feature. Individual few-layer Ti_3CN flakes are also observed, while the different transparencies indicate the various thicknesses (Figure 1e). The few-layer structure is further confirmed by the TEM image at the edge of a single flake, as shown in Figure S2. Figure 1f displays the high-resolution transmission electron microscopy (HRTEM) image of few-layer Ti_3CN, which clearly shows the crystalline lattice. The hexagonal symmetry structure is further confirmed by the selected area electron diffraction (SAED) pattern (inset in Figure 1f). Figure 1g shows an energy-dispersive X-ray spectroscopy (EDS) elemental mapping of the Ti_3CN flakes, which confirms their elemental composition. It can be noted that the copper grid is covered with an ultrathin carbon film,

https://doi.org/10.1021/acsnano.1c10577
ACS Nano 2022, 16, 3059−3069

which results in a less obvious display of the C element compared with the Ti and N ones. In order to further confirm the thickness of the as-exfoliated Ti_3CN MXene, AFM was carried out with a 512 pixel, and the sample was spin-coated on a Si/SiO_2 substrate. No liquid cascade centrifugation was used to perform the size selection. The as-exfoliated Ti_3CN MXene exhibits a large size distribution (Figure 1h). However, the thickness of the Ti_3CN flakes is uniform, as can be seen by the marked height profiles. Figure 1i demonstrates the summarized depth of the AFM image. The left peak belongs to the depth of the substrate, which has been normalized to 0 nm. The right peak refers to the depth of the Ti_3CN NSs with a distance to the substrate calculated to be ~2.6 nm, which can be regarded as the average thickness of the as-exfoliated Ti_3CN MXene. Figure 1j shows the XDR patterns of the Ti_3AlCN MAX phase and of Ti_3CN MXene. The interlayer distance has been decreased owing to the removal of the Al layer, resulting in a broadened and downshifted (002) peak of Ti_3CN. This is in good agreement with other kinds of MXenes, which implies that the MAX phase has completely converted to MXenes. Due to the exfoliation, the XRD pattern of the few-layer Ti_3CN MXenes reveals a weakening of the intense peaks, as compared with Ti_3AlCN MAX. The elemental composition is further confirmed by XPS measurements. As can be seen in Figure 1k, the elements of Ti, C, N, and O can be observed in both Ti_3AlCN and Ti_3CN, and the XPS Al 2s and Al 2p peaks disappear in Ti_3CN after HF-etching treatment, which is in good agreement with the EDS mapping results in SEM and TEM. In addition, the strong F 1s peak indicates that there are abundant −F groups on the as-fabricated Ti_3CN MXenes, which can be ascribed to the usage of the HF acid.

Photoexcited Carrier Relaxation. Nondegenerate pump−probe experiments with femtosecond time resolution were carried out to explore the excited-state dynamics of Ti_3CN NSs.[30] Compared with degenerate pump−probe measurement, more probe wavelengths (*i.e.*, more excited-state levels) dynamics can be unscrambled and explored.[29,31] In the pump−probe technique, the pump laser excites the electron transit from the low ground state to a higher excited state, and the probe laser is monitored and the change of sample's absorptivity/transmittance is recorded by the spectrometer. Generally, the intensity of the pump laser is one order higher than that of the probe laser, which precludes the influence of the probe laser. In the experiment setup, the wavelength of the pump light is fixed at 410 nm (~3 eV), which offers sufficient energy to promote electrons from the ground state to the excited state. The broadband continuum probe light constitutes two components with wavelength regimes of 490−770 nm and 840−1240 nm, which is obtained from irradiating different nonlinear crystals. Figure 2a demonstrates the 2D color transient absorption (TA) mapping of few-layer Ti_3CN NSs from visible to near-infrared wavebands. As revealed, only a broadband negative TA signal can be observed in this region, which corresponds to a ground-state bleaching (GSB) transient response. The GSB negative signal indicates the decrease of probe laser absorption, which can be attributed to the stimulation of a great amount of charge transferring to the excited state. According to the Pauli exclusion principle, the probe laser cannot absorb the electron at the ground state, resulting in a photoinduced bleaching signal.[32] This is in good agreement with the calculated absorptive cross section of ground state (σ_{gs}) and excited (σ_{es}) state, where the σ_{gs}/σ_{es} of Ti_3CN NSs is calculated to excess

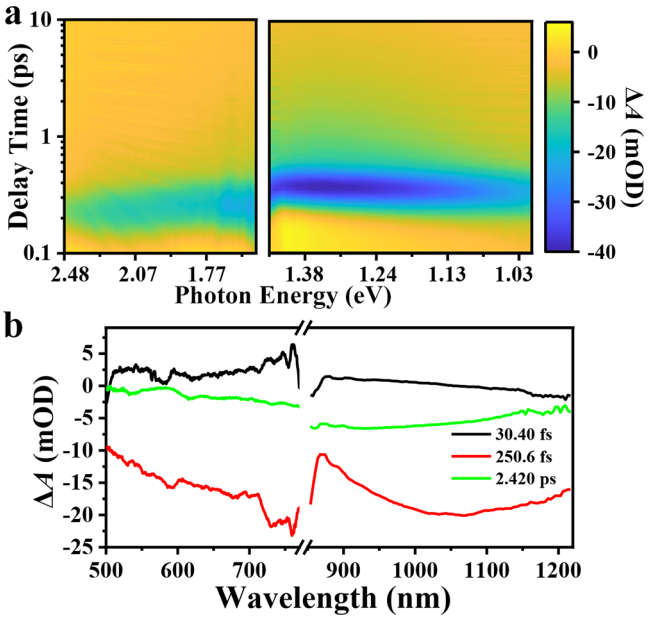

Figure 2. (a) 2D color TA mapping of few-layer Ti_3CN NSs with the probe wavelength of 500−770 and 840−1240 nm. (b) Broadband TA spectra of the few-layers Ti_3CN NSs at time delays of 30.40 fs, 250.6 fs, and 2.42 ps.

1.[33] Therefore, the negative GSB signal of Ti_3CN NSs should be from the relative stronger ground state absorption than the excited state one. A similar phenomenon has been observed in traditional semiconductors, which has been named as "dynamic Burstein Moss" effect.[34,35] As can be seen in Figure 2b, the amplitude of the TA signal reaches the maximum at 250 fs after the pump and probe light approach the NSs. Theoretically, the intensity of the TA signal at a specific wavelength is tightly related to the carrier density of the excited state. Herein, the TA signal will increase to close to zero when the carrier relaxes to the lower excited state. The time scale of the relaxation processes is in the picosecond (ps) range, implying that the Ti_3CN NSs can be applied to build ultrafast optical modulator devices. Figure 2b summarizes the TA spectra at the various time delays of 30.4 fs, 250.6 fs, and 2.42 ps. Apparently, the TA signal reduces to zero in a broadband wavelength range at the ps level, indicating an ultrafast carrier relaxation process in the Ti_3CN MXenes.

To further understand the time-related relaxation process of the few-layer Ti_3CN NSs, the dynamic curves at various probe wavelengths are fitted (Figure 3). The single pulse energy of the ultrafast pump laser is fixed at 700 nJ. A double-exponential function was applied to fit the experimental TA signals as follows:

$$\Delta A = A_1 \exp\left(-\frac{t - t_0}{\tau_1}\right) + A_2 \exp\left(-\frac{t - t_0}{\tau_2}\right) \quad (1)$$

where t refers to the delay time between pump and probe light, τ_1 and τ_2 are the estimated time constants relating with relaxation processes, t_0 is the rising time, and A_1 and A_2 represent the amplitudes of two components. The fitted data at the various probe wavelengths are shown as black solid lines in Figure 3, which are in good agreement with the experimental results. The two time constants can be attributed to the carrier−carrier scattering time and carrier−phonon scattering time, respectively. Due to the large size distribution of the

https://doi.org/10.1021/acsnano.1c10577
ACS Nano 2022, 16, 3059−3069

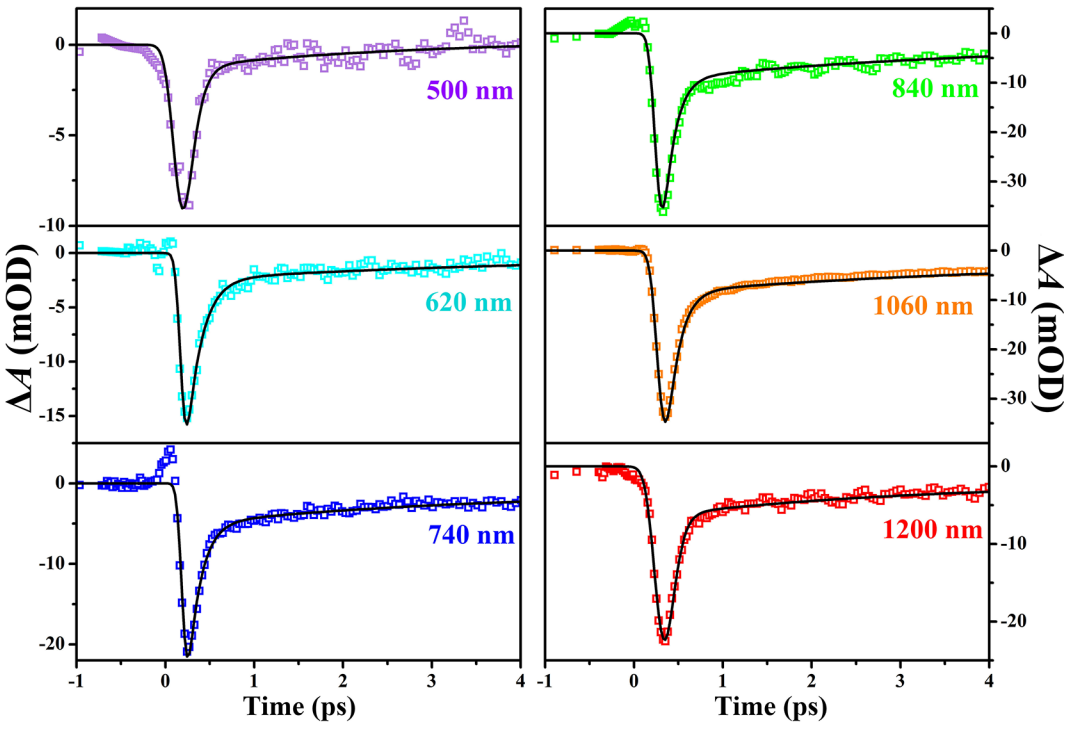

Figure 3. Dynamic curves and fitted results of the Ti_3CN NSs at 500, 620, 740, 840, 1060, and 1200 nm, respectively.

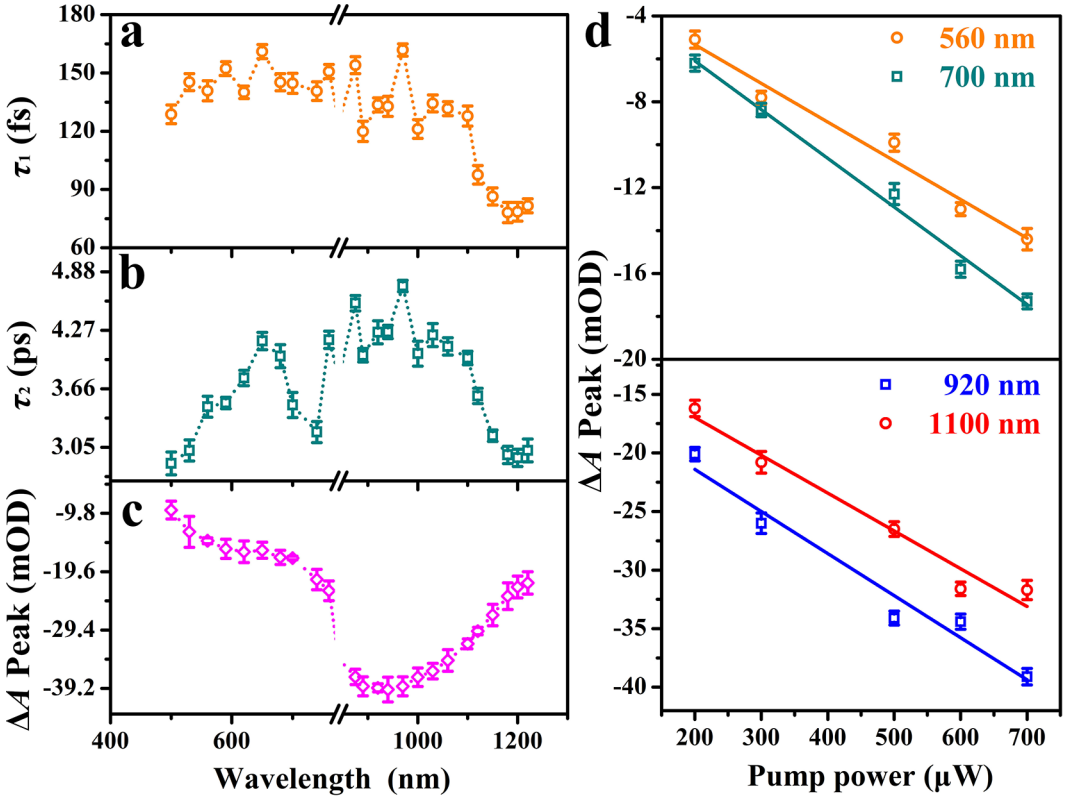

Figure 4. (a) Fast relaxation time constants against the wavelength. (b) Slow relaxation time constants against the wavelength. (c) Peak absorption against the wavelength. (d) Peak absorption against the power intensity of the pump laser under various wavelengths.

Ti_3CN NSs, the fitted results of the dynamic curves reveal the statistical results for these samples. From the TA spectra, the broadband dynamics at different delay times become apparent. For the dynamic curves in Figure 3, the signals rapidly decrease to the minimum value in ~250 fs. These ultrafast relaxation processes observed here could indicate the possibility to use Ti_3CN NSs as materials for ultrahigh-speed modulators.

Figure 4a,b summarizes the fitted time constants under different wavelengths. In the tested wavelength region, the fast time constant (τ_1) of Ti_3CN NSs is measured to range from 78

https://doi.org/10.1021/acsnano.1c10577
ACS Nano 2022, 16, 3059−3069

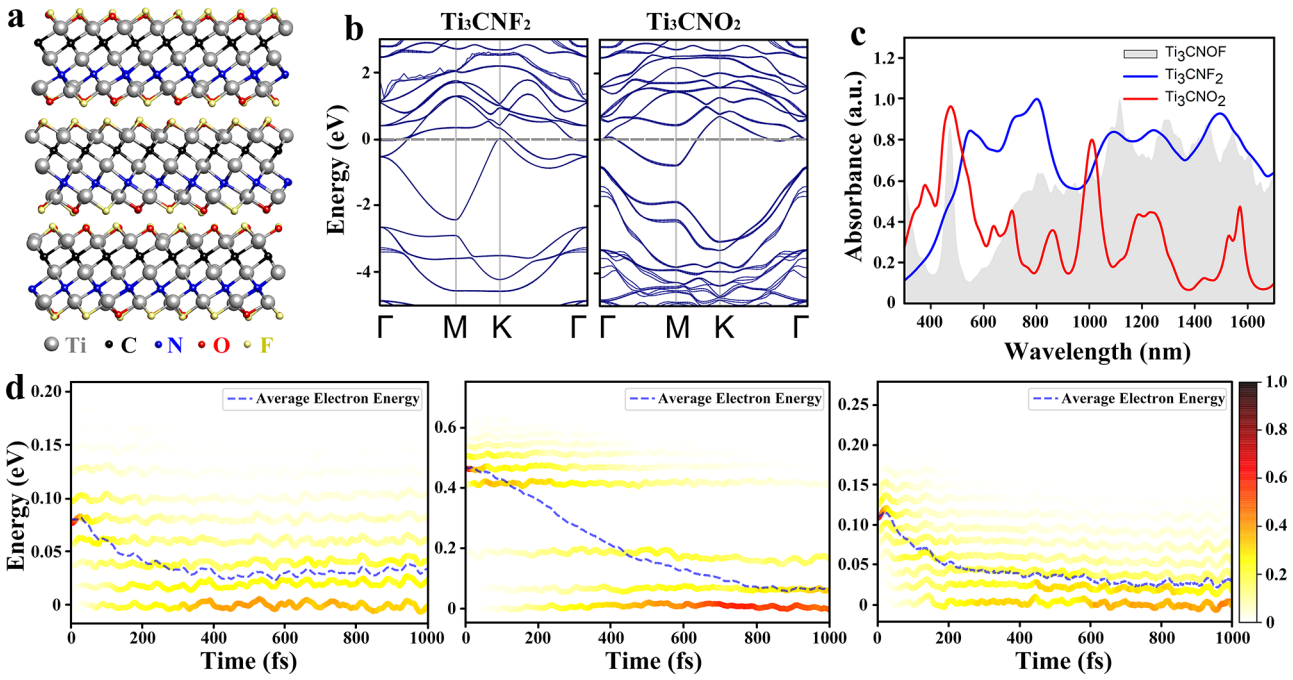

Figure 5. (a) Atomic structure of trilayer Ti_3CNOF. (b) Calculated electronic band structures of Ti_3CNT_2 NSs (T = F or O). (c) Absorption spectra Ti_3CN MXene with various terminations. (d) Time-dependent electron energy change at 300 K for O-, F-, and mixed terminated Ti_3CN from left to right.

to 160 fs, which is close to the pulse duration of the laser and can be regarded to refer to carrier−carrier scattering. The slow time constants (τ_2) are calculated at a several ps scale. For instance, τ_2 is about 2.88 and 4.25 ps at 500 and 940 nm, respectively. The slow relaxation is in the nonthermal regime, which can be attributed to the process of carrier−phonon scattering. Due to the ultrafast carrier−phonon relaxation process, the carrier relaxation process undergoes low collision probability with optical phonons. Therefore, the Ti_3CN NSs own high carrier mobility also has a proportional relationship with the carrier−phonon scattering time. We can remind that a high carrier mobility is a prerequisite for establishing high-performance optoelectronic devices. There is no obvious relationship between probe wavelength and time constants, while the fast and slow constants show an approximately consistent change tendency. Figure 4c shows the measured ΔA peak under different wavelengths. As revealed, the peak absorption increases with the increment of wavelength from 500 to 950 nm, while it decreases in the wavelength region of 950−1200 nm. Normally, the ΔA peak values are strongly associated with the carrier population of the excited state, resulting in a much smaller absorption than at other probe wavelengths. Therefore, the maximum of the ground-state bleaching signal for Ti_3CN NSs should be ~950 nm (1.31 eV). Figure 4d demonstrates the measured ΔA peak of Ti_3CN NSs against the pump power, and the fitted results are shown as solid lines. As seen, the ΔA peak increases with the increment of the pump power under various wavelengths, which can be well fitted as a linear relation. When more ground-state carriers are excited by the pump laser, the transmittance of the probe laser enhances due to the Pauli exclusion principle.

The complete photoexcited carrier relaxation dynamics of Ti_3CN NSs undergoes the following steps: (1) carrier−carrier scattering and (2) carrier−phonon scattering (Figure S3).[36−38] The Ti_3CN NSs absorb high-energy photons from the pump laser and generate a large amount of photoexcited electrons (Figure S3a). The electron relaxation processes (*i.e.*, energy dissipation processes) can occur by means of three processes. Generally, the photoexcited electrons interact with additional electrons near the Fermi level and reach electron thermalization. The photon-excited electrons rapidly form hot electrons with a Fermi−Dirac distribution by electron−electron collision, and the resultant hot electrons will achieve the same electronic temperature (Figure S3b). Then, the high-excited-state electrons mainly interact with optical phonons, since these phonons possess higher energy than the acoustic phonons. The excess energy of the optical phonon can dissipate, and the electrons lose their excess momentum, relaxing to a minimum point of the excited state. The temperature difference between electrons and optical phonons levels out, resulting in a thermal equilibrium (Figure S3c). It is notable that the lattice is also heated by inelastic collisions between carriers and phonons. Hence, optical phonons interact with other lattice modes (*e.g.*, acoustics phonons) and reach the same lattice temperature in the following 3−5 ps. In addition, the long-term stability of Ti_3CN NSs is further confirmed by the TA spectra under the irradiation of 1060 nm. For the Ti_3CN suspension stored 1 day, 7 days, and 14 days, there is neither apparent color difference nor precipitation (Figure S4a). The TA signals are almost overlapped, and a slight decrement can be observed in the enlarged region (Figure S4b), indicating that the Ti_3CN NSs are stable during the experimental section. The high stability of Ti_3CN NSs can be ascribed to the storage process, where the oxygen is removed, light is blocked, and low temperature is ensured.

To further investigate electronic and optical properties of few-layer Ti_3CN NSs, we utilized first-principle calculations and nonadiabatic molecular dynamics. Taking into account that the elemental mapping analysis confirmed the successful removal of the Al layer from the MAX phase, revealing the

https://doi.org/10.1021/acsnano.1c10577
ACS Nano 2022, 16, 3059−3069

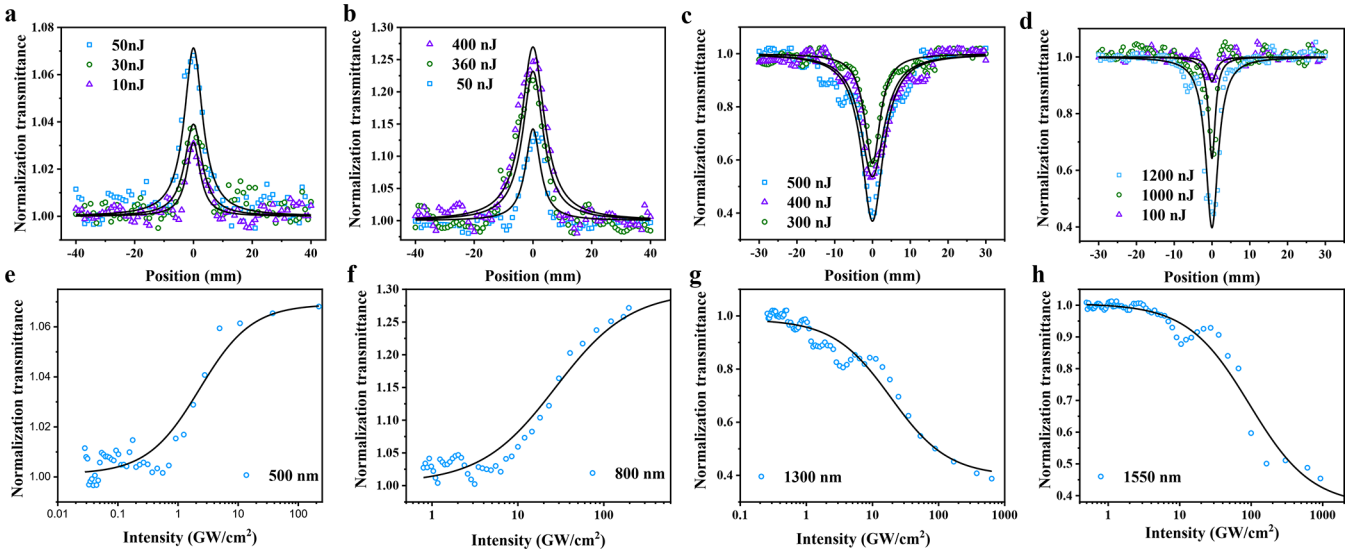

Figure 6. NLO response characteristics of Ti_3CN NSs at different single pulse energies under: (a) 500 nm, (b) 800 nm, (c) 1300 nm, and (d) 1550 nm. The normalized transmittance *versus* incident optical intensity can be found in (e−h), respectively.

absence of the Al element in Ti_3CN MXene, and that the average thickness of the as-produced MXenes is calculated to be ∼2.6 nm, we can assume that Ti_3CN MXene has a trilayer structure. The optimized structure demonstrates an average thickness of ∼2.9 nm, which is comparable to experimental data, while bilayer Ti_3CN has an average thickness <2 nm that is significantly smaller compared to the experimental results. The presence of F and O elements in the EDS analysis and the XPS spectra indicates that the most probable termination is by means of these groups. Therefore, to investigate the electronic and optical properties of Ti_3CN, we constructed three types of models with O-, F-, and mixed terminations. The optimized structure with mixed termination type is presented in Figure 5a. The band structure calculations (Figure 5b) reveal that independent of termination type, Ti_3CN demonstrates robust metallic properties, something that is in excellent agreement with other theoretical and experimental reports.[39−41] One can observe quite steep distributions of bands crossing the Fermi level that refer to the good conductivity of MXenes, while there is a relatively flat conduction band just above the Fermi level. This plays an important role in the optical properties of MXenes due to the so-called parallel band absorption effect,[42] which favors multiple absorption as discussed in the following section.

The optical spectra of O-, F-, and mixed terminated Ti_3CN are shown in Figure 5c. All spectra have a typical metallic character with large absorption in the IR range. The mixed termination can be considered as a superposition of O- and F-terminated Ti_3CN with obvious contributions from both types. We found that the transitions at around 470 nm have the most prominent oscillator strength and therefore should be considered as the most probable ones. One should note that the difference in peak intensities in the absorption spectrum between mixed Ti_3CNOF and Ti_3CNF_2/Ti_3CNO_2 is caused by contributions of both O- and F-terminated MXene bands and their relative oscillator strength, which has been normalized to 1.

In order to further investigate hot electron relaxation, we carried out nonadiabatic molecular dynamic calculations of Ti_3CN MXene with various terminations. Figure 5d demonstrates valence and conduction band evolution with time at 300 K. Thermal fluctuations of the atoms induce splitting of degenerate bands and oscillations, as shown in Figure S5. Oscillations significantly increase from F- to O-terminated MXene, while the structural evolution with time in all studied termination cases is comparable. Therefore, we can conclude that the electronic structure of Ti_3CN with an O-terminated surface is very sensitive to the thermal fluctuation of atoms. The time-dependent hot electron relaxation in the conduction band is presented in Figure 5d. The results suggest that in the case of F- and mixed O-,F-terminations, the electron energy drastically changes within the ∼200 fs losing about 80−90% of the energy. We attribute this short time period to the fast time constant (τ_1) of the Ti_3CN NSs that is measured to range from 78 to 160 fs. The photoexcited carriers are after excitation quickly converted into hot carriers with a Fermi−Dirac distribution and then cooled down by fast relaxation through electron−electron and electron−phonon scattering in the conduction band. Here, it was unexpectedly found that entirely O-terminated Ti_3CN NSs show a much slower hot electron relaxation process. This could possibly be attributed to the large density of degenerative bands in the Ti_3CNO_2 conduction band where the relaxation takes place. The thermal fluctuations break the degeneracy and create a complicated multilevel electronic structure,[43] which is responsible for capturing and storing hot electrons before they cool down to the conduction band minimum.[44]

Nonlinear Optical Response. Motivated by the fact that NLO materials are of great importance for passive optical modulators and optical limiting devices,[45] we decided to investigate the broadband NLO characteristics of Ti_3CN NSs. Here, the well-developed open-aperture (OA) Z-scan technique was applied under various wavelengths (500−1550 nm) with increased pulse power (Figure 6). The transmittance (*i.e.*, the ratio between two detectors) *versus* the position of the sample was also recorded and normalized. Figure 6 displays the OA Z-scan results at 500, 800, 1300, and 1550 nm and the fitting of these data. The corresponding nonlinear absorption curves with incident intensity are also summarized and directly inserted in Figure 6. Interestingly, the Ti_3CN NSs demonstrate

https://doi.org/10.1021/acsnano.1c10577
ACS Nano 2022, 16, 3059−3069

Table 1. Linear and Nonlinear Optical Parameters of Ti_3CN NSs and Several Typical 2D Materials

materials	wavelength (nm)	α_0 (cm^{-1})	ΔR (%)	I_s (GW/cm^2)	β (cm/GW)	NLO response	ref
Ti_3CN	800	6.908	29.24	27.51	−0.054	SA	this work
	1550	7.958	−63.5	–	0.31	RSA	
Nb_2C	800	16.2	–	98.89	−0.28	SA	38
	1550	6.25	–	–	0.30	RSA	
MoO_3	1550	0.53	17	0.32	−0.0012	SA	45
BP/IPA	800	1.55	12.4	−334.6	−0.0060	SA	46
SnS	800	–	14.8	209	−0.0027	SA	47
graphene	1030	17.1	–	170 ± 50	−(0.094 ± 0.032)	SA	48
MoS_2	800	11.22	–	381 ± 346	−(0.024 ± 0.0080)	SA	

typical positive saturable absorption (SA) under the irradiation of 500 and 800 nm ultrafast lasers, while a reverse-saturable absorption (RSA) phenomenon is perceived under 1300 and 1550 nm lasers. This phenomenon has been observed for other kinds of MXenes, such as Nb_2C and Ti_3C_2, and the conversion from SA to RSA can be ascribed to multiphoton absorption.[31,38] We remind that materials with such characteristics can potenitally be applied to build high-performance optical modulator devices for passive Q switching or mode-locking lasers.

Generally, the total absorption (α) constitutes two components, namely a linear absorption component (α_0) and a nonlinear absorption component (α_{NL}), and can be expressed by the following equations:

$$\alpha = \alpha_0 + \alpha_{NL} \tag{2}$$

$$\alpha_0 = \ln(T)/L \tag{3}$$

$$\alpha_{NL} = \beta I \tag{4}$$

where T represents the linear transmittance, L refers to the thickness of the cuvette (1 mm), β is the nonlinear absorption coefficient, and I is the light intensity. Nonlinear absorption components have proportional relationships with the incident intensity. It is notable that the incident intensity changes with the position of the sample in a Z-scan measurement setup, resulting in the variation of absorption. The nonlinear absorption coefficients have both positive (absorption increasing with increasing incident intensity) and negative (absorption decreasing with increasing incident intensity) signs. The value of β can be deduced by fitting the normalized transmittance *versus* the sample position z with the following equation:

$$T(z) = 1 - \frac{\beta I_0 L_{eff}}{2\sqrt{2}(1 + z^2/z_0^2)} \tag{5}$$

$$L_{eff} = (1 - e^{-\alpha_0 L})/\alpha_0 \tag{6}$$

$$z_0 = \pi\omega_0^2/\lambda \tag{7}$$

where I_0 is the on-focus light intensity, L_{eff} refers to the effective thickness of the sample, z_0 is the Rayleigh range of the Gaussian beam, ω_0 represents the beam waist radius, and λ is the operating wavelength. Normalized transmittance and the fitted curves at different incident wavelengths are shown in Figure 6. According to the convex lens function, the beam spot radius changes with the position at the Z-axis, which indicates the variation of incident intensity at fixed single pulse energy. Transforming the beam radius information with incident intensity, the nonlinear absorption characteristics can be more intuitively observed by using light intensity as the abscissa (inset in Figure 6). The experimental data could be well fitted by a nonlinear transmission model:

$$T(z) = 1 - \frac{\Delta R}{1 + I/I_s} - A_{ns} \tag{8}$$

where ΔR, I_s, and A_{ns} are the modulation depth, saturation intensity, and nonsaturable loss, respectively. Several key parameters (such as α_0, β, $\mathrm{Im}\,\chi^{(3)}$, ΔR, and I_s) of Ti_3CN NSs are summarized in Table 1, which also have been compared with those of other 2D materials.

The value of β is calculated to be −0.054 cm/GW by fitting the Z-scan data at 800 nm, which is significantly higher than that of other NLO materials. The high β value of Ti_3CN NSs indicates a strong nonlinear interaction between Ti_3CN NSs and the incident light. In the passive mode-locked or Q-switched laser, the modulation depth of a saturable absorber is one of the most important parameters, as it represents the modulation ability for an optical pulse. Moreover, the modulation depth dominates the laser pulse width, for example, higher modulation depths are in favor to establish shorter pulse. In addition, a smaller saturation intensity is beneficial to create a pulsed laser under small incident optical intensity. Ti_3CN NSs possess an ultrafast relaxation time, smaller saturation intensity, and higher modulation depth, which are supposed to be advantageous aspects for SA materials for visible light waveband mode-locked and Q-switched lasers. From 1060 to 1550 nm, the Ti_3CN NSs demonstrate RSA behavior, which means that they also can be applied in optical limiting devices.

For incident wavelengths ranging from 500 to 800 nm, the nonlinear optical response is revealed to show a saturable absorption behavior because of the light bleaching effect. As shown in Figure S6a, as the energy of the incident light is higher than the optical bandgap, the electrons at the ground state can readily be promoted to excited states. Further increasing the incident optical intensity, the Ti_3CN NSs can absorb more photons and more ground-state electrons are excited until all available excited energy levels are filled (see Figure S6b). According to the Pauli exclusion principle, two identical electrons cannot occupy the same excited state, which results in optical bleaching. In such circumstances, the Ti_3CN NSs cannot absorb photons and exhibit a saturable absorption behavior. As the incident laser wavelength increases, exceeding 1300 nm, the photon energy becomes smaller than the gap between the second valence band maximum (VBM-1) and the conduction band (Figure 5) and the electrons can barely be promoted to excited states by absorbing only one photon. A gap of more than 1 eV can be found between 0 and −1 eV at Γ-point of O-terminated Ti_3CN, while this gap rapidly

https://doi.org/10.1021/acsnano.1c10577
ACS Nano 2022, 16, 3059−3069

increases along other momentum vectors and therefore effectively prevents electron excitations from lower lying states. Therefore, electrons from the deep valence VBM-1 band can only be excited by absorbing one photon with higher energy than 1.0 eV (wavelength of 1240 nm), which refers to the SA phenomenon. In the absorption plot (Figure 5), one can see that the spectrum saturates at about 1300 eV, confirming the SA behavior, something that also is found in our experimental measurements. Considering F-terminated Ti_3CN, there is a small range of states with a gap narrower than 1 eV; however, these states can disappear in cases of mixed terminations. Moreover, it has been proposed that O-termination results in a more stable MXene configuration,[49] and therefore the O groups should dominate in the final material. When the photon energy is <1 eV, more than one photon is required to excite the electron, in which case an optical limiting phenomenon can be present. In this circumstance, multiphoton absorption occurs in Ti_3CN NSs with the increment of incident intensity, showing a reverse saturable absorption effect.

CONCLUSION

In this work, Ti_3CN MXenes with high quality have been successfully fabricated *via* selective etching and molecular delamination. The few-layer structure and elemental composition of Ti_3CN NSs are further confirmed by various characterization techniques. Conducted transition absorption measurements for the Ti_3CN NSs indicate a negative ground-state absorption due to the Pauli blocking. The intraband carrier relaxation dynamic has two types of processes: carrier−carrier scattering and carrier−phonon scattering. For the fast and slow relaxation times, the fitted constants range from 78 to 160 fs and from 2.88 to 4.25 ps, respectively. Moreover, the Z-scan technique revealed a dramatic NLO response conversion from saturable absorption to reversed saturable absorption owing to the multiphoton absorption effect. The corresponding carrier relaxation dynamics and NLO response of Ti_3CN MXene have been experimentally reported and theoretically investigated. Combining the experimental observations and DFT theoretical calculations, we believe our results can be instructive for the design of 2D MXene-based optoelectronic devices with high performance. Further investigations of Ti_3CN-based devices are ongoing with the perspective to fulfill some of the great expectations for these materials.

METHODS

Materials. Ti_3AlCN (~600 mesh) was purchased from Jilin 11 Technology Co., Ltd. The 40% hydrofluoric aqueous solution (HF) and 25% tetramethylammonium hydroxide (TMAOH) aqueous solution were purchased from Macklin Inc. Double-distilled deionized (DI) water was used in the whole system, and all of the chemical reagents were used as received.

Synthesis of Multilayer Ti_3CN MXene. In a 20 mL polypropylene-based beaker, 6 mL of 40% HF solution was mixed with 2 mL of DI water to obtain a 30% HF solution. One g of Ti_3AlCN powder was slowly added into the aforementioned mixture, and the solution was stirred at room temperature for 24 h. Then the superfluous HF was removed by centrifugation (10000 rpm for 10 min), and the precipitate was washed with DI water until the pH reached ~7. The precipitate was dried in vacuum for 24 h for the SEM test.

Preparation of Few-Layer Ti_3CN NSs. 0.2 g of multilayer Ti_3CN MXene was dispersed in 6 mL of TMAOH solution which was vigorously stirred for 3 days. After the delamination, the TPAOH molecules were removed by high-speed centrifugation (15000 rpm for 10 min). The precipitate was redispersed in DI water by hand-shaking. The Ti_3CN solution was further centrifuged at 3000 rpm for 15 min to precipitate the undelaminated multilayer MXene. Finally, the supernatant containing few-layer Ti_3CN NSs was collected and directly used for the following measurements. To avoid the oxidization, the MXene solution was deoxygenated by bubbling with nitrogen for 5 min. In addition, the solution was sealed in a vial without superfluous air (Figure S4a) and covered with aluminum-foil, which was then stored in refrigerator (~5 °C).

Characterization. SEM was carried out in a field emission Hitachi SU800 microscope, and the sample was immobilized directly on a conducting resin. As Ti_3CN MXene is conductive, there is no additional spraying procedure before measurement. TEM EDS, HRTEM, and SAED were performed in a FEI Tecnai G2 F30 (300 kV) instrument where the sample was immobilized on a copper grid with ultrathin carbon film. AFM was recorded in a Bruker Dimension machine with 512 pixels, and the sample was dispersed on a Si/SiO_2 wafer. XRD was obtained by a BrukerD8 instrument (λ = 0.154 nm) with voltage of 40 kV and current of 40 mA. XPS was performed on a PHI-5000 Versa Probe II instrument using monochromatic Al Kα radiation.

TA Experiment. A broadband nondegenerate TA spectrometer is applied to investigate the carrier dynamic processes of Ti_3CN NSs. In the setup, the pump laser (410 nm) is generated by nonlinear frequency conversion, and the repetition rate of pump laser is 500 Hz. The nonlinear frequency conversion processes include sum frequency, frequency doubling, beat frequency, *etc*. The broadband probe supercontinuum laser (490−770 nm and 840−1240 nm) is generated by irradiating the 800 nm laser on various crystals. The repetition rate of the probe laser is 1000 Hz. The probe laser irradiates the detector, which generates differential absorbance signal. The total probe window is 8 ns.

Z-Scan Experiment. The ultrafast pulses (repetition rate of 1000 Hz) with different wavelengths were divided in two components by a 50:50 beam splitter. One was set as the reference light beam and collected by a photodetector (PD1). The other one was injected into the sample, and the transmitted light was shaped by a convex lens and collected by another detector (PD2). When moving forward the computer-controlled stage, where the sample was fixed from −Z to Z, the absorption variation *versus* the position can be monitored based on the power variation at PD2. The transmittance of the sample is calculated from the values of the two photodetectors. The focal length of the lens is 500 mm for wavelengths of 500 and 800 nm, while it is 150 mm for wavelengths of 1300 and 1550 nm. To minimize the effect of the sample on the propagation of the beam, a thin cuvette with 1 mm length was employed, which is shorter than the Rayleigh range of the lens (2.55 mm for 800 nm according to eq 7, where ω_0 is 25.5 μm). Before measurement, a 0.5 mm ZnSe thin crystal was used to align the optical path.

Theoretical Methods. The first-principle calculations were carried out using DFT as implemented in the VASP code.[50,51] The GGA PBE[52] exchange functional, projector augmented wave[53] method, and D3 correction[54] of weak disperse interactions were utilized to solve electronic structure. The plane wave kinetic-energy cutoff was set to 500 eV. For self-consistent calculations, we used 12 × 12 × 1 *k*-points for unit cell calculations of few-layer Ti_3CN. The convergence tolerances of the force and electronic minimizations were 10^{-3} eV/Å and 10^{-5} eV, respectively. A vacuum region of >12 Å was set to avoid artificial interaction of the neighboring images along the *z* direction. Optical properties were treated time dependently within the Tamm−Dancoff approximation by solving the Casida equation.[55−57] The *ab initio* NAMD simulations were carried out using the Hefei-NAMD code,[58] which augments the VASP with the NAMD capabilities within TDDFT and with the fewest switches surface hopping method similar to that as-reported.[59,60] After the geometry optimization, a velocity rescaling algorithm was used to heat the system to 300 K. Then a 5 ps microcanonical *ab initio* molecular dynamics trajectory was generated with a time step of 1 fs. The NAMD calculations were carried out by averaging over 100 different initial configurations. For each chosen structure, 2 × 10^4 trajectories

https://doi.org/10.1021/acsnano.1c10577
ACS Nano 2022, 16, 3059−3069

for the last 2.0 ps were set. The Visualization for Electronic and Structural Analysis software[61] was used for the visualization structure.

ASSOCIATED CONTENT

Supporting Information

The Supporting Information is available free of charge at https://pubs.acs.org/doi/10.1021/acsnano.1c10577.

EDS mapping, TEM images of Ti_3CN MXene, schematic illustration of the electron relaxation processes, and schematic diagram for SA processes and RSA processes (PDF)

AUTHOR INFORMATION

Corresponding Authors

Lingfeng Gao − *College of Material, Chemistry, and Chemical Engineering, Hangzhou Normal University, Hangzhou 311121, China;* orcid.org/0000-0001-9685-2598; Email: gaolingfeng@hznu.edu.cn

Hans Ågren − *Department of Physics and Astronomy, Uppsala University, SE-75120 Uppsala, Sweden; College of Chemistry and Chemical Engineering, Henan University, Kaifeng, Henan 475004, China*; Email: hans.agren@physics.uu.se

Han Zhang − *College of Optoelectronic Engineering, Shenzhen University, Shenzhen 518060, P.R. China;* orcid.org/0000-0002-0166-1973; Email: hzhang@szu.edu.cn

Authors

Hualong Chen − *College of Optoelectronic Engineering, Shenzhen University, Shenzhen 518060, P.R. China*

Artem V. Kuklin − *Department of Physics and Astronomy, Uppsala University, SE-75120 Uppsala, Sweden; International Research Center of Spectroscopy and Quantum Chemistry (IRC SQC), Siberian Federal University, Krasnoyarsk 660041, Russia;* orcid.org/0000-0002-9371-6213

Swelm Wageh − *Department of Physics, Faculty of Science, King Abdulaziz University, Jeddah 21589, Saudi Arabia*

Ahmed A. Al-Ghamdi − *Department of Physics, Faculty of Science, King Abdulaziz University, Jeddah 21589, Saudi Arabia*

Complete contact information is available at: https://pubs.acs.org/10.1021/acsnano.1c10577

Author Contributions

[▽]These authors contributed equally to this work.

Notes

The authors declare no competing financial interest.

ACKNOWLEDGMENTS

L.G. acknowledges the National Natural Science Foundation of China (grant no. 62005177) and start-up funding from Hangzhou Normal University (Pandeng II Plan Foundation: 2021QDL036). H.Z. acknowledges the National Natural Science Foundation of China (grant nos. 61875138 and 61961136001) and the Key Project of Department of Education of Guangdong Province (no. 2018KCXTD026). H.Å. acknowledges the support from the Program of Henan Center for Outstanding Overseas Scientists (GZS2020011). A.V.K. and H.Å. thank the support by government contracts of the Ministry of Education and Science of the Russian Federation to Siberian Federal University (FSRZ-2020-0008) and the Olle Engkvist Byggmästare foundation (contract no. 212-0178). The authors would like to thank the Swedish National Infrastructure for Computing (SNIC) at the High Performance Computing Center North (HPC2N) partially funded by the Swedish Research Council through grant agreement no. 2020/3-29. S.W. and A.A.Al-G. thank the funding by the Deanship of Scientific Research (DSR) at King Abdulaziz University (no. KEP-MSc-70-130-42), and the authors acknowledge DSR for technical and financial support. The authors also acknowledge the support from Instrumental Analysis Center of Shenzhen University (Xili Campus).

REFERENCES

(1) Novoselov, K. S.; Geim, A. K.; Morozov, S. V.; Jiang, D.; Zhang, Y.; Dubonos, S. V.; Grigorieva, I. V.; Firsov, A. A. Electric Field Effect in Atomically Thin Carbon Films. *Science* **2004**, *306*, 666−669.

(2) Glavin, N. R.; Rao, R.; Varshney, V.; Bianco, E.; Apte, A.; Roy, A.; Ringe, E.; Ajayan, P. M. Emerging Applications of Elemental 2D Materials. *Adv. Mater.* **2020**, *32*, 1904302.

(3) Leng, K.; Fu, W.; Liu, Y. P.; Chhowalla, M.; Loh, K. P. From bulk to molecularly thin hybrid perovskites. *Nat. Rev. Mater.* **2020**, *5*, 482−500.

(4) Liu, C.; Wang, L.; Qi, J.; Liu, K. Designed Growth of Large-Size 2D Single Crystals. *Adv. Mater.* **2020**, *32*, 2000046.

(5) Gao, L.; Chen, H.; Wang, R.; Wei, S.; Kuklin, A. V.; Mei, S.; Zhang, F.; Zhang, Y.; Jiang, X.; Luo, Z.; Xu, S.; Zhang, H.; Agren, H. Ultra-Small 2D PbS Nanoplatelets: Liquid-Phase Exfoliation and Emerging Applications for Photo-Electrochemical Photodetectors. *Small* **2021**, *17*, No. 2005913.

(6) Gao, L.; Wang, L.; Kuklin, A. V.; Gao, J.; Yin, S.; Agren, H.; Zhang, H. A Facile Approach for Elemental-Doped Carbon Quantum Dots and Their Application for Efficient Photodetectors. *Small* **2021**, *17*, No. 2105683.

(7) Pang, J.; Mendes, R. G.; Bachmatiuk, A.; Zhao, L.; Ta, H. Q.; Gemming, T.; Liu, H.; Liu, Z.; Rummeli, M. H. Applications of 2D MXenes in energy conversion and storage systems. *Chem. Soc. Rev.* **2019**, *48*, 72−133.

(8) Zhang, X.; Lai, Z.; Ma, Q.; Zhang, H. Novel structured transition metal dichalcogenide nanosheets. *Chem. Soc. Rev.* **2018**, *47*, 3301−3338.

(9) Anasori, B.; Lukatskaya, M. R.; Gogotsi, Y. 2D metal carbides and nitrides (MXenes) for energy storage. *Nat. Rev. Mater.* **2017**, *2*, 16098.

(10) Tang, L.; Meng, X.; Deng, D.; Bao, X. Confinement catalysis with 2D materials for energy conversion. *Adv. Mater.* **2019**, *31*, 1901996.

(11) Gao, L.; Wang, R.; Kuklin, A. V.; Zhang, H.; Ågren, H. PbSe Nanocrystals Produced by Facile Liquid Phase Exfoliation for Efficient UV-Vis Photodetectors. *Adv. Funct. Mater.* **2021**, *31*, 2010401.

(12) Gogotsi, Y.; Anasori, B. The Rise of MXenes. *ACS Nano* **2019**, *13*, 8491−8494.

(13) Gao, L.; Ma, C.; Wei, S.; Kuklin, A. V.; Zhang, H.; Agren, H. Applications of Few-Layer Nb2C MXene: Narrow-Band Photodetectors and Femtosecond Mode-Locked Fiber Lasers. *ACS Nano* **2021**, *15*, 954−965.

(14) Okubo, M.; Sugahara, A.; Kajiyama, S.; Yamada, A. MXene as a Charge Storage Host. *Acc. Chem. Res.* **2018**, *51*, 591−599.

(15) Naguib, M.; Kurtoglu, M.; Presser, V.; Lu, J.; Niu, J.; Heon, M.; Hultman, L.; Gogotsi, Y.; Barsoum, M. W. Two-Dimensional Nanocrystals Produced by Exfoliation of Ti3AlC2. *Adv. Mater.* **2011**, *23*, 4248−4253.

(16) Gao, L.; Bao, W.; Kuklin, A. V.; Mei, S.; Zhang, H.; Ågren, H. Hetero-MXenes: Theory, Synthesis, and Emerging Applications. *Adv. Mater.* **2021**, *33*, 2004129.

(17) Gao, L.; Li, C.; Huang, W.; Mei, S.; Lin, H.; Ou, Q.; Zhang, Y.; Guo, J.; Zhang, F.; Xu, S.; Zhang, H. MXene/Polymer Membranes: Synthesis, Properties, and Emerging Applications. *Chem. Mater.* **2020**, *32*, 1703−1747.

(18) Jiang, X.; Kuklin, A. V.; Baev, A.; Ge, Y.; Ågren, H.; Zhang, H.; Prasad, P. N. Two-dimensional MXenes: From morphological to optical, electric, and magnetic properties and applications. *Phys. Rep.* **2020**, *848*, 1−58.
(19) Huang, W.; Hu, L.; Tang, Y.; Xie, Z.; Zhang, H. Recent Advances in Functional 2D MXene-Based Nanostructures for Next-Generation Devices. *Adv. Funct. Mater.* **2020**, *30*, 2005223.
(20) Handoko, A. D.; Steinmann, S. N.; Seh, Z. W. Theory-guided materials design: two-dimensional MXenes in electro- and photocatalysis. *Nanoscale Horiz.* **2019**, *4*, 809−827.
(21) Jhon, Y. I.; Koo, J.; Anasori, B.; Seo, M.; Lee, J. H.; Gogotsi, Y.; Jhon, Y. M. Metallic MXene Saturable Absorber for Femtosecond Mode-Locked Lasers. *Adv. Mater.* **2017**, *29*, 1702496.
(22) Naguib, M.; Mashtalir, O.; Carle, J.; Presser, V.; Lu, J.; Hultman, L.; Gogotsi, Y.; Barsoum, M. W. Two-dimensional transition metal carbides. *ACS Nano* **2012**, *6*, 1322−1331.
(23) Mashtalir, O.; Naguib, M.; Mochalin, V. N.; Dall'Agnese, Y.; Heon, M.; Barsoum, M. W.; Gogotsi, Y. Intercalation and delamination of layered carbides and carbonitrides. *Nat. Commun.* **2013**, *4*, 1716.
(24) Hantanasirisakul, K.; Gogotsi, Y. Electronic and Optical Properties of 2D Transition Metal Carbides and Nitrides (MXenes). *Adv. Mater.* **2018**, *30*, No. 1804779.
(25) Wang, Y.; Nie, Z.; Wang, F. Modulation of photocarrier relaxation dynamics in two-dimensional semiconductors. *Light Sci. Appl.* **2020**, *9*, 192.
(26) Chen, H.; Gao, L.; Qin, Z.; Ge, Y.; Khan, K.; Song, Y.; Xie, G.; Xu, S.; Zhang, H. Recent advances of low-dimensional materials in Mid- and Far-infrared photonics. *Appl. Mater. Today* **2020**, *21*, 100800.
(27) Xu, N.; Li, H.; Gan, Y.; Chen, H.; Li, W.; Zhang, F.; Jiang, X.; Shi, Y.; Liu, J.; Wen, Q.; Zhang, H. Zero-Dimensional MXene-Based Optical Devices for Ultrafast and Ultranarrow Photonics Applications. *Adv. Sci.* **2020**, *7*, 2002209.
(28) Guo, J.; Shi, R.; Wang, R.; Wang, Y.; Zhang, F.; Wang, C.; Chen, H.; Ma, C.; Wang, Z.; Ge, Y.; Song, Y.; Luo, Z.; Fan, D.; Jiang, X.; Xu, J.; Zhang, H. Graphdiyne-Polymer Nanocomposite as a Broadband and Robust Saturable Absorber for Ultrafast Photonics. *Laser Photon. Rev.* **2020**, *14*, 1900367.
(29) Gao, L.; Chen, H.; Zhang, F.; Mei, S.; Zhang, Y.; Bao, W.; Ma, C.; Yin, P.; Guo, J.; Jiang, X.; Xu, S.; Huang, W.; Feng, X.; Xu, F.; Wei, S.; Zhang, H. Ultrafast Relaxation Dynamics and Nonlinear Response of Few-Layer Niobium Carbide MXene. *Small Methods* **2020**, *4*, 2000250.
(30) Wang, K.; Szydlowska, B. M.; Wang, G.; Zhang, X.; Wang, J. J.; Magan, J. J.; Zhang, L.; Coleman, J. N.; Wang, J.; Blau, W. J. Ultrafast Nonlinear Excitation Dynamics of Black Phosphorus Nanosheets from Visible to Mid-Infrared. *ACS Nano* **2016**, *10*, 6923−32.
(31) Wang, G.; Bennett, D.; Zhang, C.; Ó Coileáin, C.; Liang, M.; McEvoy, N.; Wang, J. J.; Wang, J.; Wang, K.; Nicolosi, V.; Blau, W. J. Two-Photon Absorption in Monolayer MXenes. *Adv. Opt. Mater.* **2020**, *8*, 1902021.
(32) Miao, X.; Zhang, G.; Wang, F.; Yan, H.; Ji, M. Layer-Dependent Ultrafast Carrier and Coherent Phonon Dynamics in Black Phosphorus. *Nano Lett.* **2018**, *18*, 3053−3059.
(33) Chen, H.; Gao, L.; Al-Hartomy, O. A.; Zhang, F.; Al-Ghamdi, A.; Guo, J.; Song, Y.; Wang, Z.; Algarni, H.; Wang, C.; Wageh, S.; Xu, S.; Zhang, H. Tailoring the ultrafast and nonlinear photonics of MXenes through elemental replacement. *Nanoscale* **2021**, *13*, 15891−15898.
(34) Erskine, D. J.; Taylor, A. J.; Tang, C. L. Dynamic Burstein-Moss shift in GaAs and GaAs/AlGaAs multiple quantum well structures. *Appl. Phys. Lett.* **1984**, *45*, 1209−1211.
(35) Kamat, P. V.; Dimitrijevic, N. M.; Nozik, A. J. Dynamic Burstein-Moss shift in semiconductor colloids. *J. Phys. Chem.* **1989**, *93*, 2873−2875.
(36) Othonos, A. Probing ultrafast carrier and phonon dynamics in semiconductors. *J. Appl. Phys.* **1998**, *83*, 1789−1830.
(37) Zhang, Q.; Yan, L.; Yang, M.; Wu, G.; Hu, M.; Li, J.; Yuan, K.; Yang, X. Ultrafast Transient Spectra and Dynamics of MXene ($Ti_3C_2T_x$) in Response to Light Excitations of Various Wavelengths. *J. Phys. Chem. C* **2020**, *124*, 6441−6447.
(38) Wang, Y.; Wang, Y.; Chen, K.; Qi, K.; Xue, T.; Zhang, H.; He, J.; Xiao, S. Niobium Carbide MXenes with Broad-Band Nonlinear Optical Response and Ultrafast Carrier Dynamics. *ACS Nano* **2020**, *14*, 10492−10502.
(39) Hart, J. L.; Hantanasirisakul, K.; Lang, A. C.; Anasori, B.; Pinto, D.; Pivak, Y.; van Omme, J. T.; May, S. J.; Gogotsi, Y.; Taheri, M. L. Control of MXenes' electronic properties through termination and intercalation. *Nat. Commun.* **2019**, *10*, 522.
(40) Zhang, W.; Cheng, C.; Fang, P.; Tang, B.; Zhang, J.; Huang, G.; Cong, X.; Zhang, B.; Ji, X.; Miao, L. The role of terminations and coordination atoms on the pseudocapacitance of titanium carbonitride monolayers. *Phys. Chem. Chem. Phys.* **2016**, *18*, 4376−4384.
(41) Jhon, Y. I.; Koo, J.; Anasori, B.; Seo, M.; Lee, J. H.; Gogotsi, Y.; Jhon, Y. M. Metallic MXene saturable absorber for femtosecond mode-locked lasers. *Adv. Mater.* **2017**, *29*, 1702496.
(42) Harrison, W. A. Parallel-band effects in interband optical absorption. *Phys. Rev.* **1966**, *147*, 467.
(43) Kilina, S. V.; Kilin, D. S.; Prezhdo, O. V. Breaking the phonon bottleneck in PbSe and CdSe quantum dots: time-domain density functional theory of charge carrier relaxation. *ACS Nano* **2009**, *3*, 93−99.
(44) Wang, H.; Wang, F.; Xu, T.; Xia, H.; Xie, R.; Zhou, X.; Ge, X.; Liu, W.; Zhu, Y.; Sun, L.; et al. Slowing Hot-Electron Relaxation in Mix-Phase Nanowires for Hot-Carrier Photovoltaics. *Nano Lett.* **2021**, *21*, 7761−7768.
(45) Lin, J.; Chen, H.; Ma, D.; Gong, Y.; Li, Z.; Li, D.; Song, Y.; Zhang, F.; Li, J.; Wang, H.; Zhang, Y.; Zhang, H. Band structure tuning of alpha-MoO3 by tin intercalation for ultrafast photonic applications. *Nanoscale* **2020**, *12*, 23140−23149.
(46) Lu, S. B.; Miao, L. L.; Guo, Z. N.; Qi, X.; Zhao, C. J.; Zhang, H.; Wen, S. C.; Tang, D. Y.; Fan, D. Y. Broadband nonlinear optical response in multi-layer black phosphorus: an emerging infrared and mid-infrared optical material. *Opt. Express* **2015**, *23*, 11183−11194.
(47) Xie, Z.; Zhang, F.; Liang, Z.; Fan, T.; Li, Z.; Jiang, X.; Chen, H.; Li, J.; Zhang, H. Revealing of the ultrafast third-order nonlinear optical response and enabled photonic application in two-dimensional tin sulfide. *Photonics Res.* **2019**, *7*, 494−502.
(48) Wang, K.; Feng, Y.; Chang, C.; Zhan, J.; Wang, C.; Zhao, Q.; Coleman, J. N.; Zhang, L.; Blau, W. J.; Wang, J. Broadband Ultrafast Nonlinear Absorption and Nonlinear Refraction of Layered Molybdenum Dichalcogenide Semiconductors. *Nanoscale* **2014**, *6*, 10530−10535.
(49) Hu, T.; Li, Z.; Hu, M.; Wang, J.; Hu, Q.; Li, Q.; Wang, X. Chemical origin of termination-functionalized MXenes: $Ti_3C_2T_2$ as a case study. *J. Phys. Chem. C* **2017**, *121*, 19254−19261.
(50) Kresse, G.; Furthmüller, J. Efficient iterative schemes for *ab initio* total-energy calculations using a plane-wave basis set. *Phys. Rev. B* **1996**, *54*, 11169.
(51) Kresse, G.; Hafner, J. *Ab initio* molecular dynamics for liquid metals. *Phys. Rev. B* **1993**, *47*, 558.
(52) Perdew, J. P.; Burke, K.; Ernzerhof, M. Generalized gradient approximation made simple. *Phys. Rev. Lett.* **1996**, *77*, 3865.
(53) Blöchl, P. E. Projector augmented-wave method. *Phys. Rev. B* **1994**, *50*, 17953.
(54) Grimme, S.; Antony, J.; Ehrlich, S.; Krieg, H. A consistent and accurate *ab initio* parametrization of density functional dispersion correction (DFT-D) for the 94 elements H-Pu. *J. Chem. Phys.* **2010**, *132*, 154104.
(55) Benedict, L. X.; Shirley, E. L.; Bohn, R. B. Optical absorption of insulators and the electron-hole interaction: An *ab initio* calculation. *Phys. Rev. Lett.* **1998**, *80*, 4514.
(56) Albrecht, S.; Reining, L.; Del Sole, R.; Onida, G. *Ab initio* calculation of excitonic effects in the optical spectra of semiconductors. *Phys. Rev. Lett.* **1998**, *80*, 4510.

https://doi.org/10.1021/acsnano.1c10577
ACS Nano 2022, 16, 3059−3069

(57) Rohlfing, M.; Louie, S. G. Electron-hole excitations in semiconductors and insulators. *Phys. Rev. Lett.* **1998**, *81*, 2312.
(58) Kuklin, A. V.; Begunovich, L. V.; Gao, L.; Zhang, H.; Ågren, H. Point and complex defects in monolayer $PdSe_2$: Evolution of electronic structure and emergence of magnetism. *Phys. Rev. B* **2021**, *104*, 134109.
(59) Craig, C. F.; Duncan, W. R.; Prezhdo, O. V. Trajectory surface hopping in the time-dependent Kohn-Sham approach for electron-nuclear dynamics. *Phys. Rev. Lett.* **2005**, *95*, 163001.
(60) Akimov, A. V.; Prezhdo, O. V. The PYXAID program for non-adiabatic molecular dynamics in condensed matter systems. *J. Chem. Theory Comput.* **2013**, *9*, 4959−4972.
(61) Momma, K.; Izumi, F. VESTA 3 for three-dimensional visualization of crystal, volumetric and morphology data. *J. Appl. Crystallogr.* **2011**, *44*, 1272−1276.

https://doi.org/10.1021/acsnano.1c10577
ACS Nano 2022, 16, 3059−3069